Supplementary Material

for

Geometry of Valley Growth

Alexander P. Petroff[1], Olivier Devauchelle[1], Daniel M. Abrams[1,2],
Alexander E. Lobkovsky[1], Arshad Kudrolli[3], Daniel H. Rothman[1]

[1]*Department of Earth, Atmospheric and Planetary Sciences, Massachusetts Institute of Technology, Cambridge, MA 02139 USA*
[2]*Present address: Department of Engineering Sciences and Applied Mathematics, Northwestern University, Evanston, IL 60208*
[3]*Department of Physics, Clark University, Worcester, MA 01610*

Contents

1 Computation of the water table

In order to find the distribution of groundwater flux into the network, we solved for the shape of the water table around the channels. From the main text, the Poisson elevation ϕ of the water table is a solution to the equation:

$$\nabla^2\phi^2 + 1 = 0 \tag{S1}$$

with absorbing and zero flux boundary conditions. Thus ϕ is independent of the hydraulic conductivity K.

The ground water flux at a point is related to the shape of the watertable through the equation

$$q = \frac{K}{2}\|\nabla h^2\| \tag{S2}$$

from which

$$q = P\|\nabla\frac{K}{2P}h^2\| \tag{S3}$$

Thus, from the definition of ϕ

$$q = P\|\nabla\phi^2\| \tag{S4}$$

Because ϕ is only a function of the network geometry, q is independent of K. This result also follows from conservation of mass. The total discharge from the network must be equal to the total rain that falls into the network, regardless of conductivity. K sets the slope of watertable at the boundary required to maintain this flux.

2 Selection of the boundary

We solve the equation around a boundary chosen to follow the position of springs and streams. To identify such a boundary, we first remove the mean slope (0.0025) of the topography. We then chose the 45 m elevation contour of the resulting topography as the boundary (Figure S1) obtained from a high resolution LIDAR map of the network (*S1*). This elevation was chosen as the approximate elevation of many springs. When the contour exits the area where the LIDAR map was available, we replace the missing section of the channel with an absorbing boundary condition. Because this approximation results in uncertainties in the flux near the missing boundary, we only analyze the water flux into a well contained section of the network (blue boundary in Figure S1). Finally, we include a zero-flux boundary condition in the south east in the approximate location of a drainage divide. We solve equation (S1) with these boundary conditions using a finite-element method (*S2*).

3 Comparison of the shape of the water table to the Poisson elevation

Here we show that the solution of equation (S1) is consistent with field observations. We compare ϕ (Figure S2b) to a previously reported (*S1*) ground penetrating radar (GPR) survey of the channels (Figure S2c).

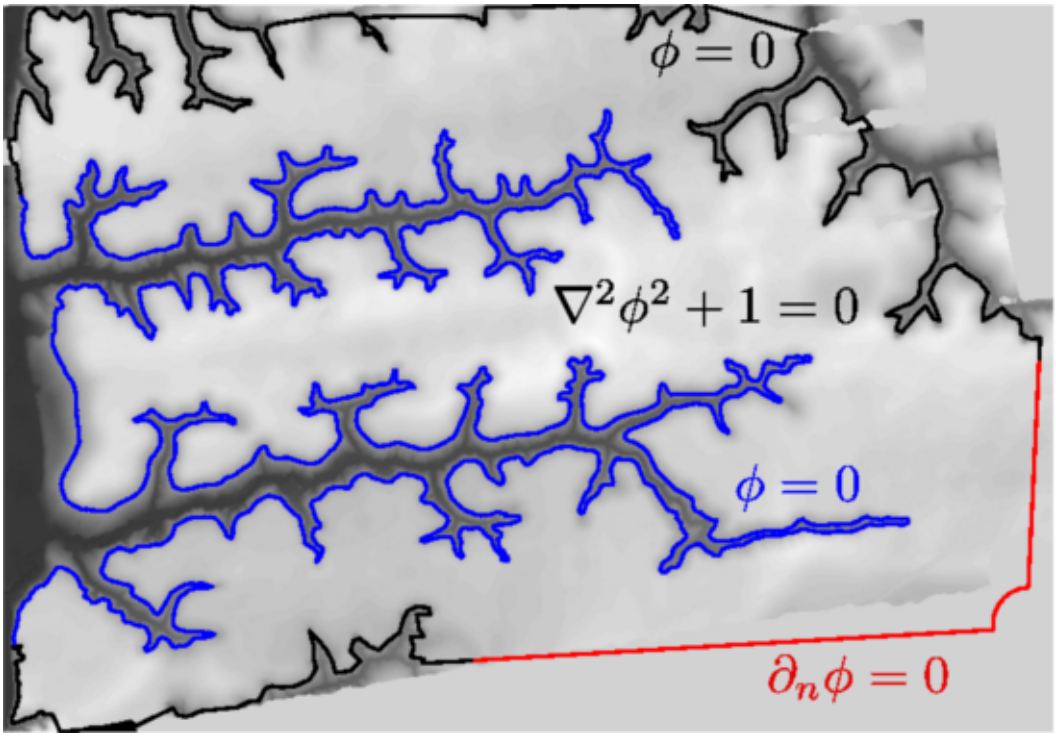

Figure S1: To most closely approximate the shape of the network we use an elevation contour of the topography. Approximating the channels as nearly flat, we required that the water table intersect the channels at a constant height, which we chose as zero. This boundary is drawn in blue and black. Additionally, a drainage divide (red line) was included in the south east. Because our LIDAR map (*S1*) only shows two full valley networks, we only analyze the data from this portion of the boundary (blue line). The boundary is linearly interpolated between points spaced at 20 m intervals on the blue boundary and points spaced by an average of 50 m on the red and black boundaries.

As all heights are measured relative to the impermeable layer, we define h_0 to be the reference elevation and shift h accordingly. It follows from the definition of ϕ that

$$h = h_0 + \sqrt{\frac{2P}{K}\phi^2 + (h_B - h_0)^2}, \tag{S5}$$

where h_B is the elevation of the water table at the boundary. A least squares fit of the measured elevations to equation (S5) gives estimates $P/K = 7 \times 10^{-5}$, $h_0 = 38$ m, and $h_B = 38$ m (figure S2d). Additionally taking P to be the observed mean rainfall rate of 5×10^{-8} m sec^{-1}, gives $K = 6 \times 10^{-4}$ m sec^{-1}. Each of these estimates is consistent with the analysis of Ref. (*S1*). Furthermore, the estimated permeability is consistent with the permeability of clean sand (*S3*). The elevation h_0 of the impermeable layer may be overestimated due to uncertainties in the analysis of the GPR data.

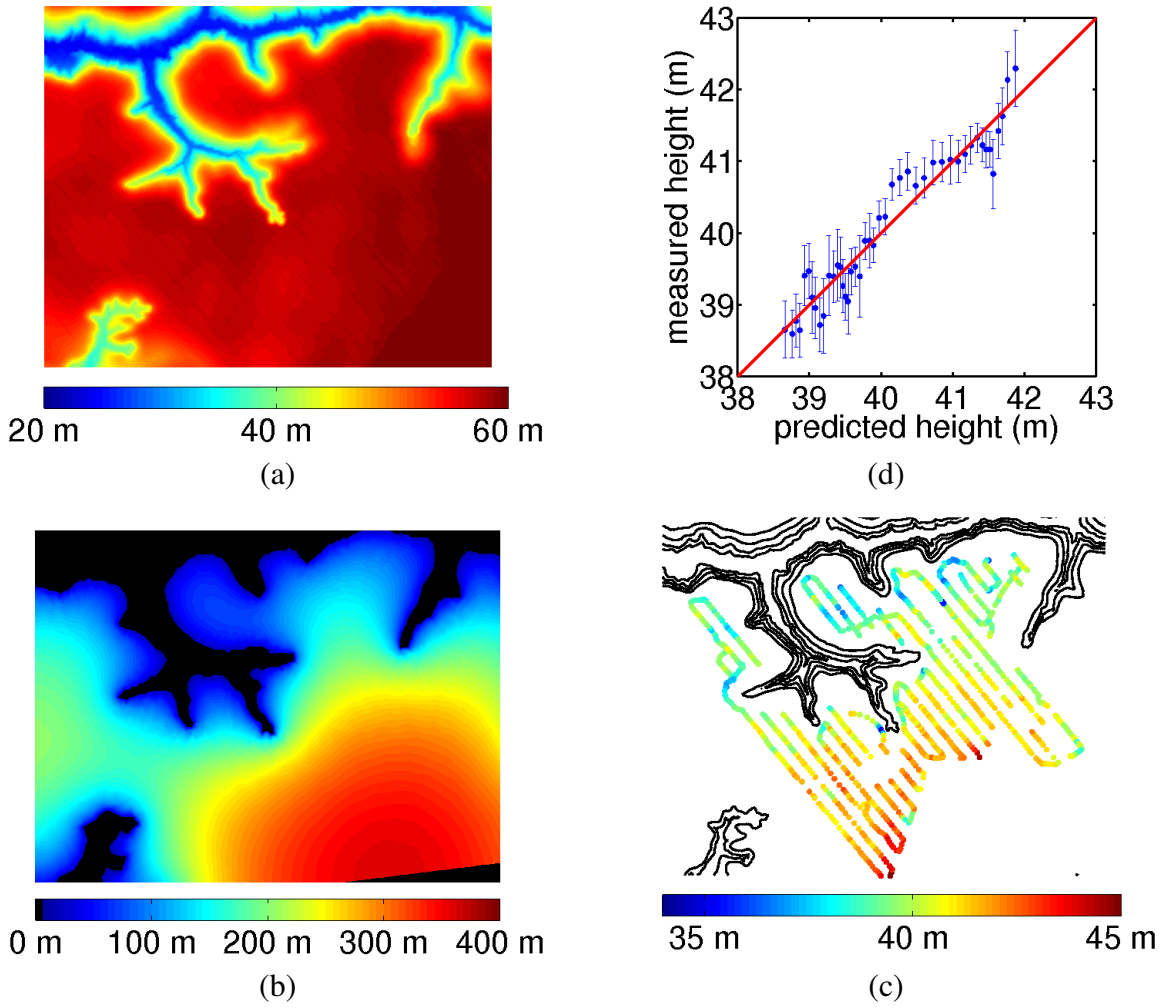

Figure S2: Comparison of the Poisson elevation to field observation. (a) The available ground penetrating radar survey was conducted on a portion of the southern valley network. The topographic map of the channels near the survey is 1400 m across. (b) We solved equation (S1) around the valley for the Poisson elevation. (c) The ground penetrating radar survey (*S1*) provided the elevation of the water table above sea level at 1144 points around the network. The valley walls are represented by the elevation contours for 30 m to 45 m at 5 m intervals. (d) The measured height is consistent with theory. The red line indicates perfect agreement.

4 Comparison of contour curvature to the groundwater flux

Because the curvature is a function of the second derivative of a curve, its estimation requires an accurate characterization of the channel shape. To have the highest possible accuracy in the estimation of curvature, we restrict the comparison between flux and curvature to a small piece of the network where the boundary is linearly interpolated between points separated by 5 m.

The curvature at a point on the boundary is computed by fitting a circle to the point and its neighbors on both sides (Figure S3b). Given the best fitting circle, the magnitude of the curvature is the inverse of the radius. The curvature is negative when the center of the circle is outside the valley and positive when the center is inside the valley.

To compare the curvature and flux at a point, we calculate the Poisson flux q_p into each section of this piece of the network by solving equation (S1) between the channels (Figure S3c). We closed the boundary on the eastern side of the domain by attaching the extremities to the valley network to the east using zero-flux boundaries. To identify the characteristic dependence of the flux at a point on the curvature, we averaged the flux and curvature at points on the boundary with similar curvatures. Each point in Figure S3d represents the average flux and curvature of 50 points on the boundary.

5 The Poisson flux-curvature relation

The Poisson flux is the area that drains into small segment of the network divided by the length of the segment. It can therefore be considered as a "local" inverse drainage density. Because all of the area drains into some piece of the channel, the integral of the Poisson flux is the total area of the basin. It follows that its mean value is the inverse drainage density.

In what follows we ask how the Poisson flux depends on the distance d a piece of the network is from its drainage divide. Proceeding from an idealization in which d has a characteristic value in a network, we find a scaling of geometric flux with curvature that is consistent with observation (Fig. 1c). To these ends we neglect interactions between valleys and note that the importance of groundwater competition has been previously considered (*S1*). Although this derivation gives some motivation for the flux-curvature relationship in the absecence of interactions, its validity is ultimatly based on observation.

A section of the network receives a large flux when it drains a large area a or when all of the water is forced through a small length of channel wall ℓ. When water from a large basin ($d \gg \kappa^{-1}$) drains toward a point , then $a \sim d^2$ (Fig. S4a). Note that "$\sim$" is the symbol for "is the order of magnitude of" or "scales as." This area is drained into a section of channel, the length ℓ of which is proportional to the planform radius of curvature, κ^{-1}; thus in regions of high curvature

$$q_p = \Omega\kappa, \tag{S6}$$

where $\Omega = md^2$ is a constant of the network related to the characteristic groundwater discharge of a head and $m \sim 1$ is a proportionality constant related to the characteristic shape of a valley head. The flux into a point is therefore proportional to the product of variables characterizing the network, Ω, and the local geometry of the channel, κ. Equating d with the inverse drainage density of the network, we find $d = 147$ m from the analysis of the topographic map. Fitting a hyperbola to the data in Fig. 1c, given this value of d, gives $m = 1.5 \pm 0.2$, consistent with $m \sim 1$.

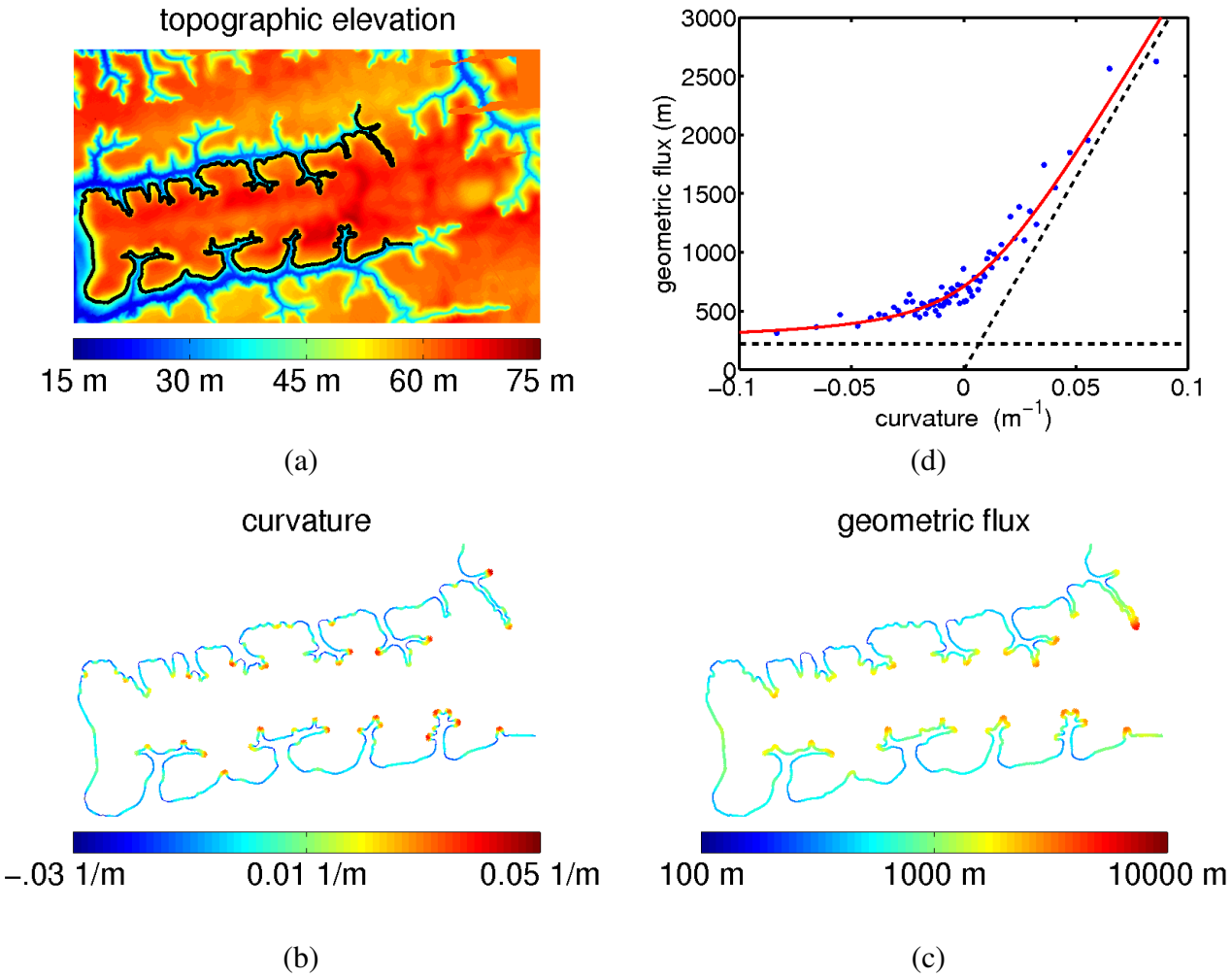

Figure S3: Identification of the relationship between the curvature of the valley walls and the local flux of groundwater. (a) The curvature and flux are measured between two valleys along the black contour. (b) The curvature at each point on the boundary is measured by fitting a circle to boundary. (c) The flux into each section of the network is found from the solution of equation (S1). (d) Comparison of the flux into each section of the network to the curvature. Geometric reasoning gives the asymptotic behavior (black dashed lines) of this relation when the magnitude of the curvature is large.

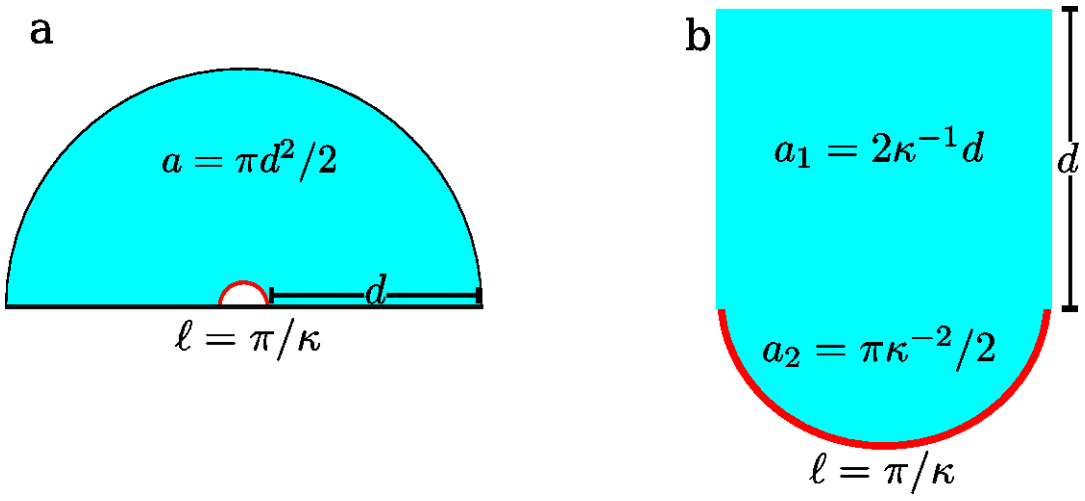

Figure S4: The Poisson flux is the local drainage density. (a) When a basin drains into a convex region (red line) the drainage density increases with curvature κ. (b) When a basin drains into a concave interval, the drainage density decreases with curvature.

In concave regions of the channel the area drained is the sum of the area outside the concavity and the area inside the concavity (Fig. S4b). This area a can be expressed as

$$a = m_1 d\kappa^{-1} + m_2\kappa^{-2}, \tag{S7}$$

where m_1 and m_2 are dimensionless numbers related to the shape of the drainage basin outside and inside the concavity, respectively. For example, if the concavity is a semi-circular depression and it drains a rectangular region, then $m_1 = 2$ and $m_2 = \pi/2$. This area is drained by a segment of length $\sim \kappa^{-1}$ giving a mean Poisson flux q_p that scales as

$$q_p = (m_1 d + m_2\kappa^{-1})/m_3, \tag{S8}$$

where m_3 is a dimensionless number related to the shape of the concavity. Fitting the data to a hyperbola, and again taking $d = 147$ m, we find $m_1/m_3 = 1.52 \pm 0.22$ and $m_2/m_3 = 10.80 \pm 2.97$. This scaling relation, in combination with the behavior at large positive κ, gives the the asymptotic behavior of the flux-curvature relation.

6 Derivation of the shape of the valley head

Here we derive equation (5) of the main text.

The balance between translation and curvature-driven growth relates the orientation to the curvature through the equation

$$\pi \cos\theta = w\kappa. \tag{S9}$$

We first re-write the orientation of a segment in terms of the local normal $\hat{n}(x)$ to the curve and the direction the head is translating $\hat{y}$. It follows from the definition of θ that

$$\pi\hat{n}(x) \cdot \hat{y} = w\kappa(x), \tag{S10}$$

Next, by describing the shape of a valley head by a curve $y(x)$, equation (S10) becomes

$$\frac{-\pi}{\sqrt{1+(\partial_x y)^2}} = w\frac{\partial_{xx} y}{(1+(\partial_x y)^2)^{3/2}}. \tag{S11}$$

With the substitution $g = \partial_x y$, this equation is re-expressed as an integrable, first order equation as

$$w\partial_x g + \pi(1+g^2) = 0. \tag{S12}$$

Integrating once,

$$g = \partial_x y = -\tan\left(\frac{\pi x}{w}\right). \tag{S13}$$

Integrating a second time for y gives

$$y = \frac{w}{\pi}\log\cos\left(\frac{\pi x}{w}\right), \tag{S14}$$

equivalent to equation (5) of the main text.

Although not necessary here, it is occasionally useful to express the shape of the channel as a vector $\mathbf{v}$ parameterized by arc length s,

$$\mathbf{v}(s) = \frac{w}{\pi}\begin{pmatrix} 2\text{arctan}(\tanh(\pi s/2w)) \\ \log(\text{sech}(\pi s/w)) \end{pmatrix}. \tag{S15}$$

The derivative $\mathbf{v}$ is the unit tangent vector.

7 Selection of valley heads

The derivation of equation (S14) requires that the channel grow forward without changing shape. Consequently, when identifying seepage valley heads suitable for analysis, we restricted our analysis to isolated channels.

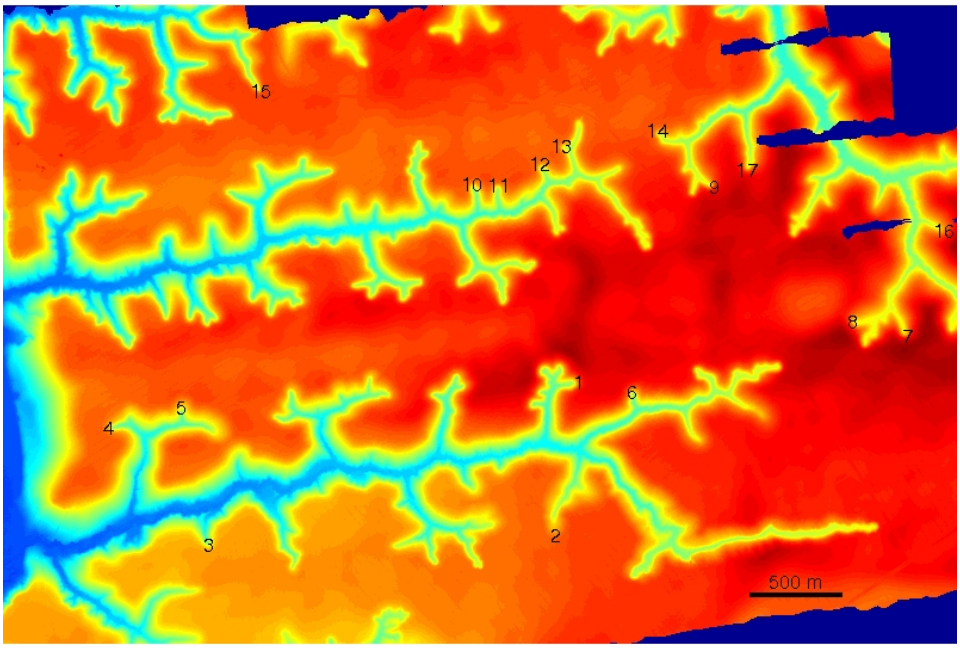

Figure S5: 17 isolated valley heads were chosen from the Florida network

7.1 Florida Network

We select valley heads from the Florida network that are reasonably isolated and not bifurcating. Given such a valley, we extract an elevation contour approximately one half the distance between the spring and the upland flat plain. We find that the deviation in the shape of any given channel from equation (S14) is insensitive to the choice of elevation contour.

Table S1: Valley heads from the Florida network. Coordinates are given with respect to UTM zone 16R

channel	Easting (m)	Northing (m)	elevation (m)	width (m)
1	696551.40	3373949.52	56.91	100.66
2	696423.49	3373123.32	55.74	111.03
3	694537.55	3373068.53	42.93	50.47
4	693995.09	3373701.11	49.49	49.60
5	694391.80	3373813.01	43.49	38.72
6	696841.09	3373900.80	44.23	28.96
7	698339.72	3374200.55	59.95	83.53
8	698040.54	3374282.69	50.91	48.28
9	697285.68	3375011.47	59.12	80.20
10	695968.97	3375029.24	49.15	56.05
11	696114.42	3375019.47	46.62	42.59
12	696336.97	3375135.23	49.88	56.34
13	696453.90	3375233.09	51.13	50.54
14	696976.13	3375317.38	51.10	46.08
15	694818.57	3375532.39	54.82	52.04
16	698537.91	3374777.58	54.21	70.77
17	697463.52	3375108.63	53.97	55.17

7.2 Experiments

The experimental apparatus used to grow seepage channels has been previously described (*S4*). The channel used in the comparison to equation (S14) grew from an initially rectangular indentation 3 cm deep in a bed of 0.5 mm glass beads sloped at an angle of 7.8° with a pressure head of 19.6 cm. To extract the shape of the channel, we first removed the slope of the bed by subtracting the elevation of each point at the beginning of the experiment. We then follow the growth of an elevation contour a constant depth below the surface. Because the shape of channel at the beginning of the experiment is heavily influenced by the shape of the initial indentation, we restrict our analysis to the shape of the contour after 45 minutes of growth. The channel grew for a total of 119 minutes and was measured at 3 minute intervals.

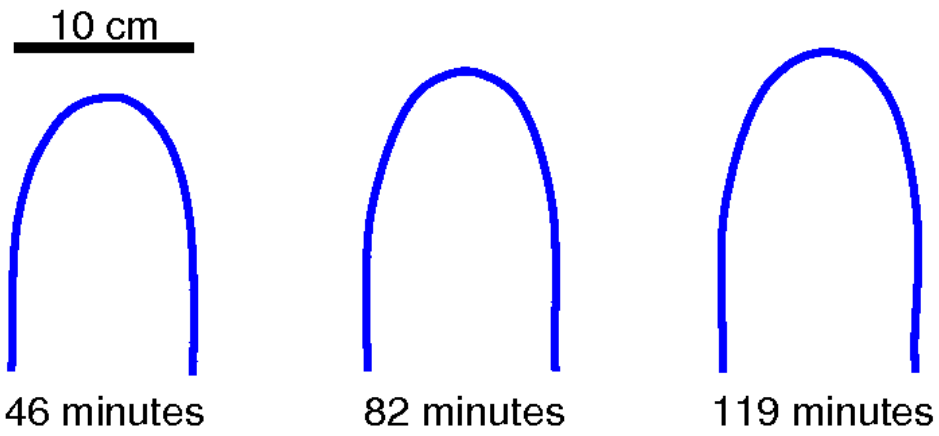

Figure S6: An elevation contour (blue lines) was extracted from the experiment every three minutes from a digital elevation map (*S5*). These three representative elevation contours from the beginning, middle, and end of the experiment demonstrate that the shape changed little during growth.

7.3 Snake River valley heads

To compare the form of amphitheater-shaped valley heads growing off of the Snake River in Idaho, we extract the valley shape from images taken from Google Earth. We select three prominent heads (Table S2, Figure S7); Box Canyon (*S6*) and two near Malad Gorge. We extract the shape of each of these heads by selecting points at the upper edge of the valley head. The mean spacing between points is 13 m. We stop selecting points when the valley turns away from the head.

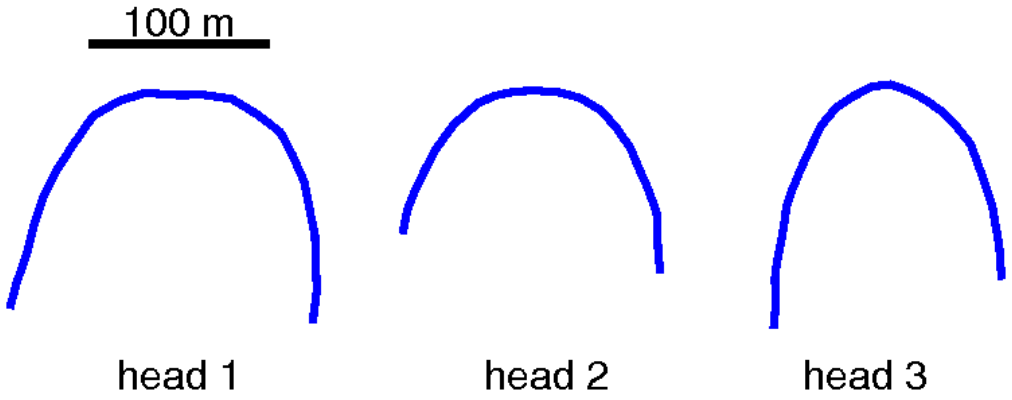

Figure S7: The shape of amphitheater-shaped valley heads growing off of the Snake River in Idaho were extracted from aerial photos of the channels. Heads 1 and 2 are near Malad Gorge. Head 3 is Box Canyon.

Table S2: Valley heads near the Snake River

channel	latitude	longitude	width (m)
1	42.8675°	115.6432°	190
2	42.8544°	115.7045°	166
3	42.7084°	114.9683°	132

7.4 Martian valley heads

The shapes of the Martian ravines which we compared to equation (S14) were extracted from images generated by the Themis camera on the Mars Odyssey orbiter. Channels are selected based on the condition that the amphitheater head was largely isolated from neighboring structures. Because the ravines are deeply incised into the topography, there is typically a sharp contrast between the ravines and the surrounding topography. We extract the shape of the ravine by selecting points spaced of order 100 m apart along the edge of the ravine (Table S3, Figure S8). We stop selecting points when the ravine intersects with a neighboring structure or when the direction of the valley curves away from the head.

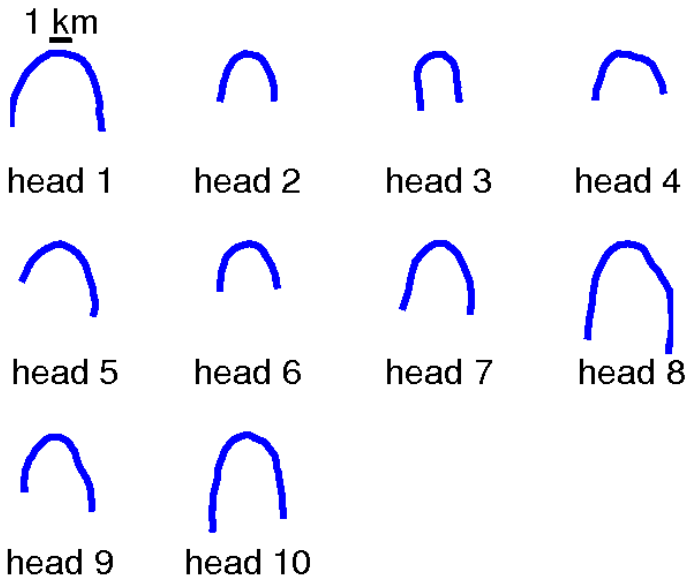

Figure S8: 10 valley heads near the Nirgal Valley, Mars. The shape of each head was extracted by selecting points at the edge of the valley head from images generated by the Mars Odyssey orbiter.

Table S3: Martian valley heads

head	Themis Image	latitude	longitude	width (m)
1	V06395001	-8.7270°	278.1572°	4730
2	V06395001	-8.7235°	278.1557°	2650
3	V09004001	-9.4310°	274.6110°	1940
4	V11138002	-7.9183°	275.4740°	3690
5	V11138002	-7.9160°	275.4736°	3740
6	V14133002	-9.5763°	278.4435°	2940
7	V14857001	-7.5656°	273.6060°	3110
8	V16654002	-8.7792°	275.5868°	3970
9	V16654002	-8.7781°	275.5894°	3310
10	V26750003	-8.0633°	274.8977°	3370

8 Stream discharge data

8.1 Comparison of field measurements to the predicted flux

Fig. 1 of the main text compares the solution of equation (S1) to field measurements. The instantaneous discharge of a stream is measured from the the cross-sectional area a in a locally straight section of the channel and the surface velocity v, from which the discharge $Q = av$. We measure the surface velocity of the stream from the travel time of a small passive tracer between points at a fixed distance. This method may underestimate the discharge in very small streams where a substantial fraction of the flow may be moving through the muddy banks of the stream.

To compare the measured discharge to the Poisson equation, we integrate the flux, $q = P\|\nabla\phi^2\|$, along the section of the network upstream from the measurement assuming the reported annual rainfall, $P = 5 \times 10^{-8}$ m sec^{-1}. When discharge is measured near a spring, the flux is integrated around the valley head.

8.2 January 2009

Easting (m)	Northing (m)	discharge (cm^3 sec^{-1})	predicted discharge (cm^3 sec^{-1})
696905.45	3374708.15	11700	4802.54
695425.47	3374595.35	310	422.30
695333.80	3374486.16	1900	1459.50
695410.03	3374422.51	2100	1403.02
695589.53	3374413.20	2000	1272.90
695608.45	3374439.65	1700	1145.17
695602.26	3374467.29	4700	2103.67
695532.14	3374764.77	310	490.24
694045.68	3373713.71	710	1708.72
694102.24	3373742.47	850	1381.31
694110.98	3373726.59	850	3520.83
694393.38	3373788.44	810	1761.83
694515.20	3373714.30	2300	2051.40
694700.99	3373494.69	2900	1831.06
697174.63	3373662.18	700	3004.36
697622.18	3374045.11	10800	4700.85
697523.57	3374034.52	440	2225.53
696432.08	3373937.74	3500	2619.48
696353.61	3374006.59	3500	2688.01
696415.16	3373979.53	3600	2545.77
696363.79	3373884.98	570	673.20
696314.56	3373838.46	3100	1132.34
695400.74	3373894.43	2800	2117.42
695417.69	3373884.87	3100	2522.08
694429.25	3374329.77	700	1145.16
694541.01	3374318.70	1250	1626.34
694295.68	3374320.27	700	950.41
694081.94	3374205.31	1950	2969.80
693696.69	3373094.27	300000	284251.54
693575.95	3374496.41	100000	148834.48

8.3 April 2009

Easting (m)	Northing (m)	discharge (cm^3 sec^{-1})	predicted discharge (cm^3 sec^{-1})
696577.00	3375064.00	26688	17558.21
696515.00	3375060.00	31324	25683.40
696526.00	3375081.00	10878	7960.94
696378.00	3375075.00	3155	2196.50
696374.00	3375047.00	31168	28808.33
696312.00	3374949.00	44714	33750.34
693684.21	3374490.78	181142	148233.29
693857.70	3374480.17	134261	134367.19
694237.23	3374550.07	159510	123111.22
694371.93	3374575.91	96597	120688.53
694445.52	3374574.44	123230	115351.89
694706.00	3374606.66	142841	111689.91
694808.19	3374666.05	133061	103032.24
694815.26	3374674.12	24251	14558.59
695449.36	3374792.20	70782	70543.57
695317.14	3374776.63	115771	82714.80
695400.81	3374783.02	18354	10476.11
695613.16	3374808.59	46630	69195.87
695756.20	3374863.59	11422	10024.07
695787.02	3374851.22	81630	57339.57
695914.95	3374827.10	24757	41590.16
695922.74	3374822.92	31480	15071.30
696011.72	3374871.04	6903	2472.52
696019.12	3374873.43	52090	38588.88
696127.23	3374876.96	44644	36223.61
696267.06	3374905.73	51745	34747.90
696335.93	3374970.34	52171	29296.08
696577.00	3375064.00	26688	17558.21
696515.00	3375060.00	31324	25683.40
696526.00	3375081.00	10878	7960.94
696378.00	3375075.00	3155	2196.50
696374.00	3375047.00	31168	28808.33
696346.42	3374960.48	8141	4287.83
696916.41	3374703.37	2704	2773.16
696913.37	3374697.05	2131	1230.01
695406.38	3373894.53	6791	2117.42
695284.53	3373820.41	4975	6209.90
695268.73	3373828.01	12171	7245.29
695207.06	3373539.81	28499	16435.07
695163.07	3373472.73	285299	214562.12
695825.64	3373844.08	20009	6515.55

Easting (m)	Northing (m)	discharge (cm^3 sec^{-1})	predicted discharge (cm^3 sec^{-1})
695818.15	3373874.10	3098	1747.84
695829.40	3373872.17	6847	4724.56
695870.78	3373925.80	1292	1436.14
695873.99	3373937.31	7298	2562.84
694804.18	3374918.55	4777	2926.35
694811.43	3374929.34	15554	10799.79
694864.00	3374985.35	9906	7942.65
694853.04	3375015.85	6866	2769.17
694999.62	3375057.93	11789	6421.11
695043.10	3375092.62	3376	2175.13
695043.00	3375070.20	5248	3776.13
695410.00	3373885.00	4173	2590.45
697528.00	3374024.00	995	2400.35
695529.00	3374749.00	685	490.24
695437.00	3374602.00	263	422.30
695434.00	3374600.00	10759	9777.40

References

S1. Abrams, D. M. *et al.* Growth laws for channel networks incised by groundwater flow. *Nature Geoscience* **28**, 193–196 (2009).

S2. Hecht, F., Pironneau, O., Le Hyaric, A. & Ohtsuka, K. Freefem++ Manual (2005).

S3. Bear, J. *Hydraulics of groundwater* (McGraw-Hill New York, 1979).

S4. Schorghofer, N., Jensen, B., Kudrolli, A. & Rothman, D. H. Spontaneous channelization in permeable ground: theory, experiment, and observation. *Journal of Fluid Mechanics* **503**, 357–374 (2004).

S5. Lobkovsky, A. E., Smith, B. E., Kudrolli, A., Mohrig, D. C. & Rothman, D. H. Erosive dynamics of channels incised by subsurface water flow. *J. Geophys. Res* **112** (2007).

S6. Lamb, M. P., Dietrich, W. E., Aciego, S. M., DePaolo, D. J. & Manga, M. Formation of Box Canyon, Idaho, by megaflood: Implications for seepage erosion on Earth and Mars. *Science* **320**, 1067 (2008).